

Nonclassical effects in plasmonics: An energy perspective to quantify nonclassical effectsWei Yan^{*} and N. Asger Mortensen[†]*Department of Photonics Engineering, Technical University of Denmark, DK-2800 Kongens Lyngby, Denmark and Center for Nanostructured Graphene, Technical University of Denmark, DK-2800 Kongens Lyngby, Denmark*

(Received 26 November 2015; revised manuscript received 19 February 2016; published 28 March 2016)

Plasmons are commonly interpreted with classical electrodynamics, while nonclassical effects may influence the dynamics of plasmon resonances as the plasmon confinement approaches the few-nanometer scale. However, an unambiguous approach to quantify the degree of nonclassical dynamics remains. We propose a *nonclassical-impact parameter* (NCI) to characterize the degree of nonclassical effects from an energy perspective, i.e., which fraction of the total electromagnetic energy is attributed to classical electrodynamic terms and which fraction is correspondingly to be assigned to nonclassical degrees of freedom? We show that the NCI relates directly to two fundamental parameters of plasmon resonances: the loss function and the quality factor. Guided by the NCI, we discuss the nonclassical effects of plasmon waveguiding modes of metallic slab waveguides, and highlight the general features of the nonclassical effects at different microscopic levels by contrasting the numerical results from the semiclassical hydrodynamic Drude model (HDM) and the microscopic random-phase approximation (RPA). The formal relation between the HDM and the RPA is also established for metals by exploring the limit of an infinite work function.

DOI: [10.1103/PhysRevB.93.115439](https://doi.org/10.1103/PhysRevB.93.115439)**I. INTRODUCTION**

Plasmon resonances, collective oscillations of a free-electron gas against a positive ion background, are subject to significant attention [1–5]. Plasmon resonances, including both localized-plasmon resonances and plasmon waveguiding modes, can confine electric fields beyond the optical diffraction limit [2]. This leads to numerous applications such as cancer therapy [6], nanophotonics circuits [7,8], nanolasers [9,10], and quantum information processing [11]. The majority of these developments rely on our insight from classical electrodynamics where the Drude model for the intraband plasmonic response of metals stands as a cornerstone [1,4]. This celebrated approach explains noble-metal plasmon phenomena extremely well for plasmonic structures with characteristic dimensions well above 5–10 nm [12]. However, the maturing nanofabrication allows the realization and exploration of yet smaller feature sizes [13–17]. When approaching the few-nanometer or even subnanometer scale, an increasing importance of nonclassical degrees of freedom (i.e., beyond the Drude model) can be anticipated, and with increasing weights [18]. Examples of such nonclassical degrees of freedom include the kinetics associated with the finite compressibility of the quantum electron gas [19,20] and the inhomogeneous microscopic equilibrium distribution of the quantum electron gas in the vicinity of a surface [21–23]. In Maxwell's equations, such aspects modify the local Drude permittivity to a generalized nonlocal form [24]. With respect to different nonlocal models, such as the semiclassical hydrodynamic Drude model (HDM) and the microscopical random-phase approximation (RPA), the commonly employed Drude model is also referred to as the local-response approximation (LRA).

In recent years, efforts have been directed to theoretically [20,24–31] and experimentally [13,14,32–38] investigating

nonclassical effects of plasmon resonances in metals and with interesting extensions to two-dimensional (2D) plasmonic materials such as graphene [39–41]. In addition to the fundamental interest in quantum-plasmonic phenomena, we note that quantum-electronic control may open new avenues in applications of nanoscale light confinement [18] and plasmon-induced hot electrons [42,43]. For resonant phenomena, the nonclassical effects usually manifest in broadening and shifting of plasmon resonances [32,34,44–47]. In turn, nonclassical effects also smear singularity phenomena predicted by the Drude model, such as perfect imaging [48], nanofocusing [49,50], and the field enhancement at the center of a touching dimer [51,52] that would otherwise be singular [53]. Nonclassical dynamics may also be associated with phenomena without any classical counterparts, such as the multipole surface-plasmon resonances at the interface of simple metals [47], the charge transfer plasmon resonances for dimers with subnanometric gaps [14,15,26,27,30,35], and the quantized bulk-plasmon resonances above the plasma frequency [54].

The theoretical understandings of nonclassical effects of plasmon resonances usually employ the semiclassical HDM [24,49,51,52,55–57], the RPA [39–41,58], or the time-dependent density-functional theory (DFT) [26,29,47,59,60]. Elevating us beyond these different models, it is interesting to ask if we can introduce a measure to quantify the degree of nonclassical contributions to the plasmon dynamics. One immediate candidate at hand is to associate such a parameter with the resonance shift of plasmon modes when compared to the LRA. Obviously, this would work for well-developed resonances existing within the LRA, while it would not help to appreciate quantum plasmon phenomena not holding classical counterparts. To address a broader variety of nonclassical phenomena, we here propose a *nonclassical-impact parameter* (NCI) to characterize the nonclassical effects from a total energy ($U_T = U_C + U_{NC}$) perspective: $NCI \equiv 2U_{NC}/(U_C + U_{NC})$, where $NCI = 0$ for classical (C) dynamics, while $NCI = 1$ for entirely nonclassical (NC) dynamics. As a key

^{*}wyanzju@gmail.com[†]asger@mailaps.org

result we show that

$$\text{NCI} = 1 + \frac{\text{Im}[\varepsilon_{\text{PR}}^{-1}]}{Q_{\text{PR}}} \quad (1)$$

where Q_{PR} is the quality factor of the plasmon resonance while $-\text{Im}[\varepsilon_{\text{PR}}^{-1}]$ is the loss function; both established quantities in the fields of plasmonics and electron energy loss spectroscopy of plasmons [61].

The remaining part of the paper is organized as follows: In Sec. II, with the HDM as the starting point, we partition different forms of the energies of plasmon resonances including the contributions from the nonclassical effects. Based on the energy considerations in Sec. II, we define the NCI to characterize the nonclassical effects beyond the HDM assumption in Sec. III. In Sec. IV, we discuss the relation between the NCI and the electron-pressure wave, and demonstrate the fundamental upper limit of the NCI for plasmon waveguiding modes in the HDM. In Sec. V, with the NCI, we investigate in detail the nonclassical effects by numerical analysis of plasmon waveguiding modes of metallic slab waveguides. In Sec. VI, the formal relation between the HDM and the RPA is discussed in the limit of an infinite work function. In Sec. VII, a summary and conclusions are given. Some details of our derivations are left for Appendices A, B, and C.

II. NONCLASSICAL KINETICS IN THE HYDRODYNAMIC DRUDE MODEL

We start by introducing the HDM to describe the free-electron gas. In short, the HDM seeks to account for the finite compressibility of the quantum electron gas by incorporating a pressure term in the equation-of-motion of electrons subject to electromagnetic fields. Commonly, Thomas-Fermi theory is used to describe the nonclassical (quantum) freedom of the kinetic energy, which arises from the statistical distribution of the free-electron gas, e.g., the Fermi-Dirac statistics in equilibrium. The internal kinetic energy per particle is proportional to $\max\{E_F, k_B T\}$, where E_F is the Fermi energy, while $k_B T$ is the characteristic thermal energy. For metals such as sodium, aluminum, silver, and gold, with the Fermi velocity v_F around 10^6 m/s and the effective electron mass close to the electron rest mass, we typically have $E_F \gg k_B T$ at room temperatures [19], and consequently the nonclassical kinetic energy is governed by E_F . In the present paper, we focus our attention on the above mentioned metals. In the HDM, the classical Drude model is accompanied by an additional diffusion-like gradient term [20],

$$\mathbf{J}_e = \sigma_D \mathbf{E} - \frac{i\omega\beta^2}{\omega^2 + i\omega\gamma} \nabla \rho_e. \quad (2)$$

Here, \mathbf{J}_e and ρ_e denote the electric current density and the electric charge density, respectively. Furthermore, γ is the damping rate and $\sigma_D = i\varepsilon_0\omega_p^2/(\omega + i\gamma)$ is the classical Drude conductivity with ω_p being the plasma frequency. The parameter β , associated with the nonclassical kinetic energy, has the expression $\beta^2 = v_F^2(3\omega/5 + i\gamma/3)/(\omega + i\gamma)$ [62], and gives the strength of the nonlocal relationship between \mathbf{E} and \mathbf{J} . The HDM is usually combined with the assumptions of a uniform equilibrium electron density and an infinite

work function. The two assumptions lead to (1) all material parameters in Eq. (2), i.e., σ_D , γ , and β , are set to the bulk values of the corresponding metal; (2) an additional boundary condition is imposed, i.e., the vanishing of the normal component of \mathbf{J}_e at the metal surface [20,63].

Before proceeding, we note that the HDM constitutes a lowest-order correction of the LRA to include nonlocal effects due to the finite compressibility of the quantum electron gas. Apart from recent generalizations [64–66], the HDM still neglects several important microscopic effects, including the inhomogeneity of the equilibrium electron density and its related correction to the nonclassical kinetic energy, and the electron spill-out. Nevertheless, the main motivation here of employing the HDM is to illustrate how the nonclassical degrees of freedom are modifying the dynamics of plasmons. This insight also leads us to our introduction of the NCI. At a later stage, the assumptions associated with the HDM will be relaxed.

Now, consider an arbitrary free-electron gas embedded in a dielectric background with a relative permittivity ε_d (possibly varying in space). In the electrostatic limit, the electromagnetic fields associated with plasmon resonances respect [67]

$$\int dv [\mathbf{E}\mathbf{D}^* + \mathbf{E}^*\mathbf{D}] = 0.$$

Utilizing Eq. (2), the above identity yields

$$U_K = U_E + U_{\text{NC}}, \quad (3a)$$

with

$$U_K = \frac{1}{4} \int dv_m n_0 m_e |\mathbf{v}|^2, \quad (3b)$$

$$U_E = \frac{1}{4} \int dv \varepsilon_0 \varepsilon_d |\mathbf{E}|^2, \quad (3c)$$

$$U_{\text{NC}} = \frac{1}{4} \int dv_m \frac{\beta^2 |\rho_e|^2}{\varepsilon_0 \omega_p^2}. \quad (3d)$$

Here, $\int dv_m$ is the spatial integration performed over the volume of the free-electron gas, with n_0 being the equilibrium electron density, while m_e is the effective electron mass. We note that the same expressions can also be derived from the Poynting theorem [68]. The total energy U_T and the classical energy U_C are

$$U_T = U_K + U_E + U_{\text{NC}}, \quad U_C = U_K + U_E. \quad (3e)$$

The physical meanings of $U_{K,E,NC}$ are indicated by their expressions. In particular, U_K is the time average of the classical kinetic energy of the free-electron gas, and U_E relates with the energy of the electric field. U_{NC} is the nonclassical part of the energy. To appreciate the nonclassical nature of U_{NC} , we consider a free-electron gas with a density $n = n_0 + n_1 \cos(\omega t)$, where n_0 and n_1 are two constants with n_1 being a small perturbation. Assuming that electrons are obeying Fermi-Dirac statistics, the system has the nonclassical energy density $3nE_F/5$. Accordingly, the time average of the nonclassical kinetic energy density W_{NC} contributed from the dynamic perturbation n_1 is

$$W_{\text{NC}} = \frac{m_e v_F^2 |n_1|^2}{12n_0} + \mathcal{O}(n_1^4/n_0^4).$$

In the limit where $\omega \ll \gamma$ with $\beta^2 \simeq v_F^2/3$, one finds $U_{\text{NC}} = \int dS_m W_{\text{NC}}$ by recalling that $\rho_e = -en_1$ and $\omega_p^2 = n_0 e^2 / (m_e \epsilon_0)$. This directly reveals the nonclassical origin of U_{NC} . If on the other hand $\omega \gg \gamma$ with $\beta^2 \simeq 3v_F^2/5$, then $U_{\text{NC}} \simeq 9/5 \int dS_m W_{\text{NC}}$. Here, the prefactor 9/5 is deviating from 1 owing to the fact that the Fermi-Dirac statistics no longer applies as $\omega \gg \gamma$ [69].

III. NONCLASSICAL-IMPACT PARAMETER

A. Definition and semiclassical HDM considerations

The total energy of the plasmon resonance is given by Eq. (3a). The Drude model invokes the LRA and is entirely classical, i.e., $U_{\text{NC}} = 0$. Plasmon resonances are characterized by the harmonic energy transfer between the classical kinetic energy of free electrons and the electric field energy of the whole system, in analogy with optical resonances in dielectrics with the energy transfer between the electric field energy and the magnetic energy [70]. Including the nonclassical degrees of freedom, U_{NC} has a final share of the total energy, and this modifies the classical plasmon dynamics accordingly.

Based on the above energy perspective, we here introduce the *nonclassical-impact parameter* (NCI) that we already highlighted in the Introduction:

$$\text{NCI} \equiv \frac{2U_{\text{NC}}}{U_C + U_{\text{NC}}} = 1 - \frac{2U_E}{U_T}. \quad (4)$$

In the classical Drude model, $\text{NCI} = 0$ as a direct result of $U_{\text{NC}} = 0$. Including the nonclassical effects in the HDM, NCI deviates from 0, and more specifically becomes a positive value. In the limiting case $U_E \rightarrow 0$ or equivalently $U_T \gg U_E$, we have $\text{NCI} \rightarrow 1$. In a hydrodynamic description this limit corresponds to the regime where plasmons are fully longitudinal oscillations, i.e., electron-pressure waves, as discussed in the next section. The NCI is bounded between 0 and 1. The larger value of the NCI, the more noticeable nonclassical effects.

As an example, we consider a metallic slab waveguide embedded in a free-space background medium. For simplicity we consider a lossless ($\gamma = 0$) free-electron metal with material parameters $\omega_p = 5.9$ eV and $v_F = 10^6$ m/s (corresponding to sodium). Figure 1(a) depicts the dispersions of the symmetric surface plasmon waveguiding modes (PWMs) for waveguide widths of both $d = 5$ nm and $d = 1$ nm, contrasting both the LRA classical Drude model (dash-dotted lines) and the HDM (solid lines). The wave number k_{pw} of the waveguide mode is normalized by the Fermi wave number k_F and likewise, the frequency ω is conveniently normalized by the plasma frequency ω_p . In the Drude model, k_{pw} shows a linear relation with $1/d$, indicating that k_{pw} can be increased to any value without limitations by decreasing d . In the HDM, such linear relation is broken due to nonlocal effects which cut off the large- k_{pw} divergence (see Ref. [57] for details). Accordingly, there is a ceiling to k_{pw} (a maximal permitted value of k_{pw}), as we will discuss in the next section. Figure 1(b) plots the NCI predicted by the HDM as a function of the frequency ω . It is seen that the NCI follows a trend similar to that of the wave number k_{pw} in Fig. 1(a). In particular, the NCI dramatically increases as ω exceeds the classical

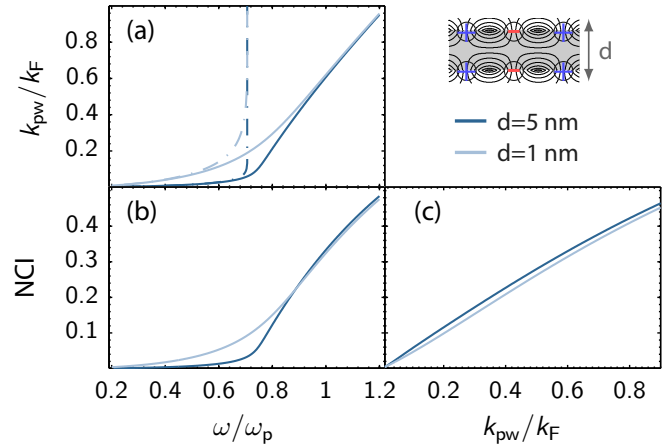


FIG. 1. The nonclassical effects for the symmetric surface PWMs of a metallic slab waveguide (of widths $d = 1$ nm and 5 nm) embedded in a free-space background. (a) Dispersion relations within the HDM and the LRA classical Drude model are plotted as the solid lines and the dash-dotted lines, respectively. (b) The NCI illustrated as a function of the plasmon frequency. (c) The NCI illustrated as a function of the plasmon wave number. The upper right inset illustrates the mode profile of the symmetric surface PWM. The metal has the material parameters $\omega_p = 5.9$ eV and $v_F = 10^6$ m/s.

surface-plasmon frequency $\omega_p/\sqrt{2}$. Below this frequency the plasmon field is predominantly of a transverse nature in good accordance with the LRA, while it turns gradually more longitudinal beyond this frequency. Figure 1(c) depicts the NCI as a function of k_{pw} . The NCI increases as the k_{pw} increases. This directly illustrates how its nonclassical nature increases as k_{pw} becomes larger. The observation can be directly understood from Eq. (2) where the nonclassical term, i.e., the gradient term, is roughly proportional to k_{pw} .

As another example, we consider the NCI for the generic problem of a free-electron metallic sphere embedded in free space. Using a Mie formulation of the HDM [71], we find to lowest order in the particle radius R that the NCI for localized plasmon resonances directly manifests the nonlocal blueshifting with

$$\begin{aligned} \text{NCI} &= \frac{\Delta\omega}{\omega_{\text{LRA}}} + \mathcal{O}\left(\frac{\beta^2}{\omega_p^2 R^2}\right) \\ &= \frac{\sqrt{(\ell+1)(2\ell+1)}}{2} \frac{\beta}{\omega_p R} + \mathcal{O}\left(\frac{\beta^2}{\omega_p^2 R^2}\right). \end{aligned}$$

Here, ω_{LRA} is the plasmon resonance frequency in the LRA limit ($\omega_{\text{LRA}} = \omega_p/\sqrt{3}$ for the dipole resonance with $\ell = 1$), $\Delta\omega$ is the HDM frequency blueshift with respect to ω_{LRA} , and $\ell = 1, 2, \dots$ is the angular momentum number of the plasmon resonance. This is a quite intuitive, but also remarkable result which in turn shows how the loss function, the quality factor, and the nonlocal blueshift constitute mutually linked quantities, i.e., $\Delta\omega/\omega_{\text{LRA}} \simeq 1 + \text{Im}[\epsilon_{\text{PR}}^{-1}]/Q_{\text{PR}}$ [see Eq. (1) or the following subsection for definitions of ϵ_{PR} and Q_{PR}]. For numerical illustrations, we consider a metallic sphere put in a free-space background, and the material properties of the metal are as in Fig. 1. The values of the NCI as a function

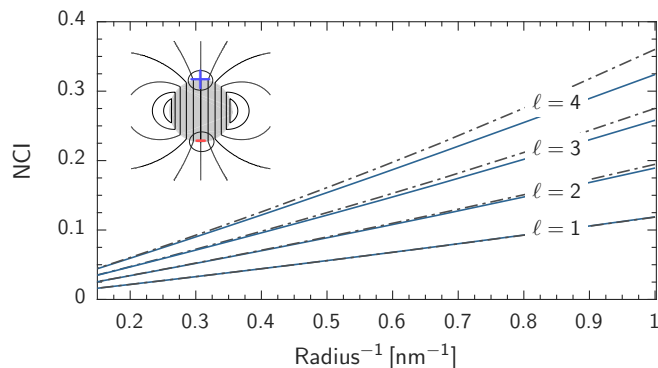


FIG. 2. The nonclassical effects for the surface plasmon modes of a metallic sphere embedded in a free-space background. The solid lines show the NCI as a function of the reciprocal of the sphere radius for the surface plasmon modes with $\ell = 1, 2, 3, 4$, where ℓ represents the angular momentum number of the plasmon mode. The dash-dotted lines give the normalized nonlocal blueshifting $\Delta\omega/\omega_{\text{LRA}}$ of the plasmon modes. The inset illustrates the mode profile with $\ell = 1$. The material parameters of the metal are the same as in Fig. 1.

of the reciprocal of the sphere radius for the surface plasmon modes with $\ell = 1, 2, 3, 4$ are plotted in Fig. 2 (solid lines). It is seen that the NCI increases its value as the radius decreases and also the angular momentum number ℓ increases. Additionally, we also depict the normalized nonlocal blueshifting $\Delta\omega/\omega_{\text{LRA}}$ of the plasmon modes (dash-dotted lines). The values of the NCI and $\Delta\omega/\omega_{\text{LRA}}$ are close to each other especially when the sphere radius is large, agreeing with the above analytical analysis.

B. Microscopic RPA considerations

Above, we used the semiclassical HDM as our starting point for our introduction of the NCI. However, our energy considerations (involving U_{E} and U_{T}) go beyond this particular model. Thus, the NCI can also be derived for microscopic quantum models, where more subtle nonclassical effects can be included. Here, we turn to the random-phase approximation as the most common way of calculating the electromagnetic response with a starting point in the single-electron eigenstates of the equilibrium system. In the RPA, the exchange-correlation contributions to the plasmon dynamics are omitted. We note that, for our metals of interest with only modest electronic correlations, the induced error is of only quantitative rather than qualitative character.

To discuss the NCI in the RPA, we introduce the spectral representation of the dielectric function operator $\epsilon(\omega)$ with [41,59,60]

$$|\phi_{\text{tot}}\rangle = \epsilon^{-1}(\omega)|\phi_{\text{ext}}\rangle,$$

where $|\phi_{\text{ext}}\rangle$ and $|\phi_{\text{tot}}\rangle$ represent the states of the external incident and resulting total electric potentials, respectively. Here, $\epsilon(\omega) = \mathbf{I} - V\chi_0(\omega)$, where V is the Coulomb interaction operator defined by $\langle \mathbf{r}|V|f\rangle = -\int d\mathbf{r}' e^2 \langle \mathbf{r}'|f\rangle / 4\pi\epsilon_0 |\mathbf{r} - \mathbf{r}'|$, and $\chi_0(\omega)$ is defined by $\langle \mathbf{r}|\chi_0(\omega)|f\rangle = \int d\mathbf{r}' \chi_0(\omega, \mathbf{r}, \mathbf{r}') \langle \mathbf{r}'|f\rangle$, where χ_0 is the noninteracting response function constructed from the single-electron orbitals of the underlying equilibrium system.

Plasmon resonances are associated with the poles of $\epsilon(\omega)^{-1}$. In particular, they are the eigenstates of $\epsilon(\omega)$

$$\epsilon(\omega)|\phi_n\rangle = \epsilon_n(\omega)|\phi_n\rangle$$

with $\epsilon_n(\omega)$ being zero. However, due to the loss, e.g., the electron-momentum relaxation associated with electron-phonon scattering and the electron-hole pair excitations, the pole will be slightly away from the real axis in the complex frequency plane. Since this complicates the evaluation of the complex-valued resonance frequency, we here make the simplification to focus on the real part of the frequency (where ϵ_n has a complex value). We define plasmon resonances in a loose mathematical sense as the eigenstates with the loss function $-\text{Im}[\epsilon_n(\omega)^{-1}]$ exhibiting a local spectral peak [41,59,60]. Those plasmon resonance (PR) eigenstates and eigenvalues are specifically denoted as $|\phi_{\text{PR}}\rangle$ and ϵ_{PR} , respectively. The loss function $-\text{Im}[\epsilon_{\text{PR}}^{-1}]$ is a common concept in electron microscopy of plasmons [61] where it quantifies the ability of external free carriers (such as a focused electron beam in an electron microscope where the swift electrons act as the sources of $|\phi_{\text{ext}}\rangle$) to couple to plasmons and in this way dissipate energy. Within the above framework, we find that the NCI can be expressed in a rather elegant form, Eq. (1), that is

$$\text{NCI} = 1 + \frac{\text{Im}[\epsilon_{\text{PR}}^{-1}]}{Q_{\text{PR}}},$$

comprising the loss function $-\text{Im}[\epsilon_{\text{PR}}^{-1}]$ and the quality factor Q_{PR} , which characterizes the plasmon resonance lifetime. For the details of the derivation we refer to Appendix A. Again, we emphasize that in this way our new measure of quantum effects is related directly to long-established key quantities for plasmon resonances; quantities that can in principle be evaluated by various methods and techniques ranging all the way from microscopic theories and *ab initio* approaches over semiclassical models to even experiments measuring the far-field optical spectra and electron energy loss spectra of plasmon resonances.

Note that compared to Eq. (4), the form of Eq. (1) no longer involves U_{T} , for which we do not find a simple expression in the RPA, while quite conveniently the quality factor and the loss function can be evaluated (see Appendix A for details).

Since we have arrived at Eq. (1) with more general arguments, the expression is also valid for the classical Drude model and the semiclassical HDM, since both models represent different levels of approximations of the RPA. In particular, the classical Drude model is the local-response approximation of the RPA, while the HDM is a k^2 approximation (k being the wave number of the electric potential after the Fourier transformation) of the RPA. Thus, Eq. (1) offers a generic recipe to quantify the nonclassical effects.

As an immediate consequence of Eq. (1), we have (in agreement with Ref. [67])

$$Q_{\text{PR}} = -\text{Im}[\epsilon_{\text{PR}}^{-1}] \quad (\text{within the LRA}) \quad (5)$$

since the Drude model is classical and $\text{NCI} = 0$ within the LRA. As an example, consider the bulk plasmon resonance for a homogenous free-electron gas. In the classical Drude model, the dielectric function operator $\epsilon(\omega)$ is simply the Drude permittivity $\epsilon_{\text{M}} = \epsilon_{\text{B}} - \omega_{\text{p}}^2 / (\omega + i\gamma)$, where ϵ_{B} is the

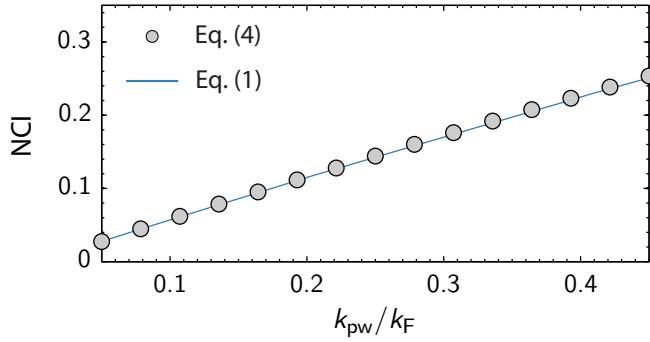


FIG. 3. Equivalence between Eq. (1) (solid line) and Eq. (4) (data points) illustrated by HDM calculation of the NCI for a symmetric surface PWM of a metallic 5 nm slab embedded in a free-space background. The material parameters of the metal are the same as in Fig. 1. A phenomenological damping rate $\gamma = 0.032\omega_p$ is added when using Eq. (1), while the damping is neglected when evaluating Eq. (4).

permittivity contributed from the bound electrons and is assumed to be dispersionless. At the bulk plasmon resonance $\omega = \omega_p/\sqrt{\epsilon_B}$, $\epsilon_{PR} = \epsilon_M/\epsilon_B$, and accordingly there is $-\text{Im}[\epsilon_{PR}^{-1}] = \omega_p/(\sqrt{\epsilon_B}\gamma)$, which also gives the value of the quality factor Q_{PR} according to Eq. (5). Thus, our considerations are, for the LRA, in perfect line with the elegant treatment of plasmon resonances in Ref. [67]. Further, to confirm the equivalence between Eqs. (4) and (1), we use the HDM to calculate the NCI of the symmetric surface PWM for a metallic slab waveguide embedded in a free-space background. The material parameters of the metal are the same as in Fig. 1, and for the width of the waveguide we consider 5 nm. The results are plotted in Fig. 3, where we observe that the values of the NCI from either Eq. (4) or Eq. (1) agree perfectly with each other.

In this section, the NCI is firstly introduced based on the HDM in the lossless case. Then, we generalize the NCI to the RPA framework, where the material losses are included. We note that the material losses in the HDM are simply described by a phenomenological parameter γ , and do not invite any new forms of energy to plasmon dynamics. Thus, the NCI in the HDM is nearly independent of γ . This is confirmed by our numerical example in Fig. 3, where it is seen that the values of the NCI from Eq. (4) with $\gamma = 0$, and Eq. (1) with $\gamma = 0.032\omega_p$ agree each other almost perfectly. Further increasing γ to $0.1\omega_p$, we numerically observe that the NCI nearly stays unchanged (not shown in Fig. 3). In the RPA theory, a new damping channel due to the electron-hole (e-h) pair excitations is self-consistently included, which offer a new degree of freedom to the nonclassical effects beyond the HDM picture. Intuitively, we expect that the e-h pair excitations can contribute to the NCI, which will be discussed in Sec. V A.

IV. NONCLASSICAL-IMPACT PARAMETER AND ELECTRON-PRESSURE WAVES

In this section, we return to the HDM and discuss the NCI in the context of longitudinal plasmon excitations. In the limiting case with $U_E \ll U_T$, we have $\text{NCI} \rightarrow 1$ as indicated by Eq. (4). In this case, plasmon resonances exhibit a harmonic energy

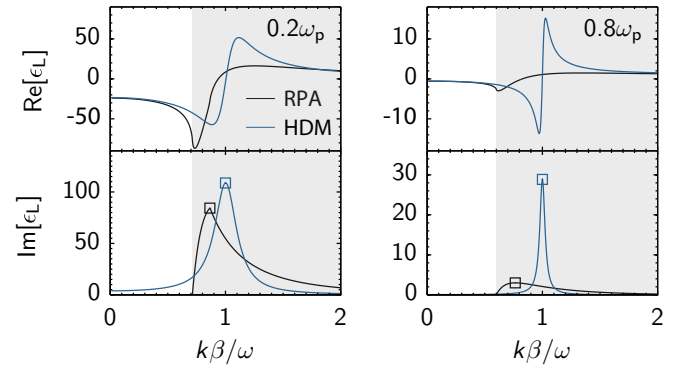


FIG. 4. Comparison of the longitudinal permittivities within HDM and LRA at $\omega = 0.2\omega_p$ (left panels) and $\omega = 0.8\omega_p$ (right panels). The material parameters are as in Fig. 1, while using $\gamma = 0.032\omega_p$ in the HDM. The squares mark the positions of k_p while shaded regions represent the RPA intraband electron-hole continuum.

transfer mainly between U_K and U_{NC} , but with negligible U_E . Consequently, the electric field term in Eq. (2) can be simply neglected. Then, by applying the gradient operator to Eq. (2) we get

$$(\nabla^2 + k_p^2)\rho_e = 0, \quad k_p = \frac{\omega}{\beta}. \quad (6)$$

The solutions to Eq. (6) are charge-density waves that we shall here refer to as *electron-pressure waves* since the nonclassical gradient term in Eq. (2) is commonly referred to as the pressure term of the free-electron gas [69]. Thus, as $\text{NCI} \rightarrow 1$, the linear-response dynamics of the free-electron gas has the property of an electron-pressure wave.

As mentioned above, the HDM is the k^2 approximation of the RPA of a homogenous electron gas. Consequently, it is important to see whether the value of k_p predicted by the HDM is close to that of the RPA. In this context, we observe that the longitudinal permittivity in the HDM is given by

$$\epsilon_L = 1 - \frac{\omega_p^2}{\omega^2 - \beta^2 k^2 + i\omega\gamma}.$$

Clearly, k_p is nothing but the resonance pole of ϵ_L if $\gamma = 0$. Within the RPA this inspires us to extract k_p in a similar way by solving for the resonance of ϵ_L . As an example, we consider a metal with properties as in Fig. 1. The left panel of Fig. 4 depicts ϵ_L as a function of k at $\omega = 0.2\omega_p$ for both the HDM and the RPA. The shaded regions represent the intraband e-h pair continuum, which contributes to the imaginary part of ϵ_L in the RPA. In the HDM, a phenomenological damping $\gamma = 0.032\omega_p$ is added. Clearly, for both the HDM and the RPA, ϵ_L exhibits the typical resonance features: the abrupt sign change of $\text{Re}[\epsilon_L]$ accompanied by a peak in $\text{Im}[\epsilon_L]$. The latter feature is now employed to identify the resonance position (marked by squares), i.e., the value of k_p . We see that k_p in the RPA is close to that in the HDM with $k_p^{\text{RPA}} = 0.865k_p^{\text{HDM}}$. The right panel of Fig. 4 depicts ϵ_L as a function of k at $\omega = 0.8\omega_p$. Comparing with the case of $\omega = 0.2\omega_p$, we emphasize two observations: (1) k_p in the RPA deviates more from that in the HDM with $k_p^{\text{RPA}} = 0.75k_p^{\text{HDM}}$; (2) the resonance of the electron-pressure wave in the RPA is more damped due to the enhanced e-h pair excitations. In summary, the k_p predicted by

the HDM is qualitatively accurate and compares well with the RPA, especially in the low-frequency regime.

In Fig. 3, we observe that the NCI increases as the PWM wave number k_{pw} grows. Thus, it is reasonable to conjecture that the ceiling to k_{pw} should correspond to the limiting case $\text{NCI} = 1$, i.e., dynamics characteristic of an electron-pressure wave. This immediately suggests the following relation:

$$k_{pw} \leq k_p. \quad (7)$$

For a slab metallic waveguide in a homogenous dielectric background, Eq. (7) has been demonstrated explicitly by analyzing the dispersion equation [63]. It has also been shown that such a ceiling is responsible for the limiting value of the photonic density of states of layered hyperbolic metamaterials [63]. Here, based on the arguments from the energy perspective, Eq. (7) is provided without any detailed specifications of either the underlying waveguide geometry or the embedding medium's dielectric properties. This suggests that Eq. (7) should be universally valid within the HDM, which is rigorously proven in Appendix B. To allow k_{pw} to approach k_p , Fig. 1 tells us that one should either make the waveguide's transverse dimensions small or alternatively aim for the high-frequency regime. However, even if the waveguide would hypothetically be as thin as one atomic layer, k_{pw} would still be far away from k_p , as will be demonstrated in the next section. Additionally, in the high-frequency regime, the enhanced loss due to the e-h pair excitations can reduce the plasmon lifetime greatly (as observed in Fig. 4), which would make experimental observations difficult. In this sense, the fundamental ceiling defined in Eq. (7) is perhaps not posing a real practical limitation in the presence of realistic damping, but it rather serves as a theoretical concept manifesting the more ultimate limitation associated with the spatial dispersion of electron-pressure waves and their nonclassical kinetic energy.

V. NUMERICAL ANALYSIS

The HDM invokes the following approximations and assumptions: (a) the k^2 approximation of the RPA; (b) a uniform equilibrium electron density; (c) an infinite work function. To investigate the nonclassical effects beyond these simplifications, we here employ the microscopic RPA for numerically analyzing the PWMs of metallic slab waveguides.

The RPA automatically lifts the k^2 approximation inherent to the HDM. Procedures to further relax the remaining approximations and assumptions will depend on the particular choice of the single-electron potential V_{el} . Here, two different models for V_{el} are considered. One approach is the infinite work function (IFW) potential well, in which $V_{el} = 0$ inside the metal, i.e., the region occupied by the jellium ion background, while $V_{el} \rightarrow \infty$ outside the metal, as illustrated in the left inset of Fig. 5. In this case, the assumption of the uniform electron density is relaxed. This allows for Friedel oscillations in the equilibrium electron density, while quantum spill-out is suppressed due to the IWF (for an early application of the infinite-barrier idea to plasmons, see Ref. [72]). The other choice involves a single-electron potential V_{el} treated self-consistently within DFT—a more accurate description [73], as illustrated in the right inset

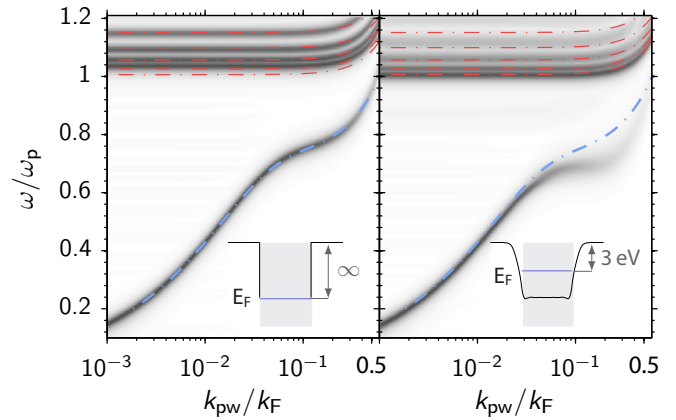


FIG. 5. Dispersions of the symmetric PWMs for a metallic 5-nm-wide slab waveguide embedded in free space. The results are computed within the HDM (dash-dotted lines), the IFW-RPA (left) and the DFT-RPA (right). The material parameters of the metal are chosen as in Fig. 1.

of Fig. 5. In the DFT, the local-density approximation of the exchange-correlation energy is employed. In this case, the assumptions of the uniform electron density and the infinite work function are both elevated. In the following, our comparison of the two RPA descriptions (the IFW-RPA and the DFT-RPA) and the HDM will exhibit nonclassical effects of plasmon resonances at different microscopic levels.

A. Metallic slab

Figure 5 depicts the dispersions of the symmetric PWMs for a metallic slab of width 5 nm, contrasting the results from the HDM (dash-dotted lines), the IFW-RPA (left), and the DFT-RPA (right). In the DFT, we employ the jellium approximation for the ion lattices, and self-consistently obtain a work function of 3 eV (see the inset of the right part of Fig. 5). The material parameters of the metal are as in Fig. 1, while a phenomenological damping rate $\gamma = 0.032 \omega_p$ is included. For the IFW-RPA and the DFT-RPA, we illustrate the largest values of the loss function $-\text{Im}[\epsilon_n^{-1}]$ (see Sec. III B) divided by the frequency, whose local peaks represent the PWMs. The demonstrated PWMs include both the surface PWMs and the bulk PWMs above ω_p .

We focus on the surface PWMs (the mode of the low-frequency branch). The results of the HDM and the IFW-RPA agree with each other. This indicates the quantitative agreement between the two models when it comes to characterizing the properties of the surface screening of the free-electron gas. This will be further discussed in Sec. VI. For the DFT-RPA, the predicted surface PWMs exhibit (1) redshifting with respect to the HDM and IFW-RPA and (2) more damping as k_{pw} increases. These two observations are attributed to the electron spill-out permitted by a finite work function. In particular, the increased damping is related to the enhanced e-h pair excitations near the jellium boundary (surface scattering) due to the electron spill-out, as recently discussed in Refs. [22,23].

To quantify the nonclassical effects, we next compute the NCI. Figure 6 depicts the NCI for the surface PWMs

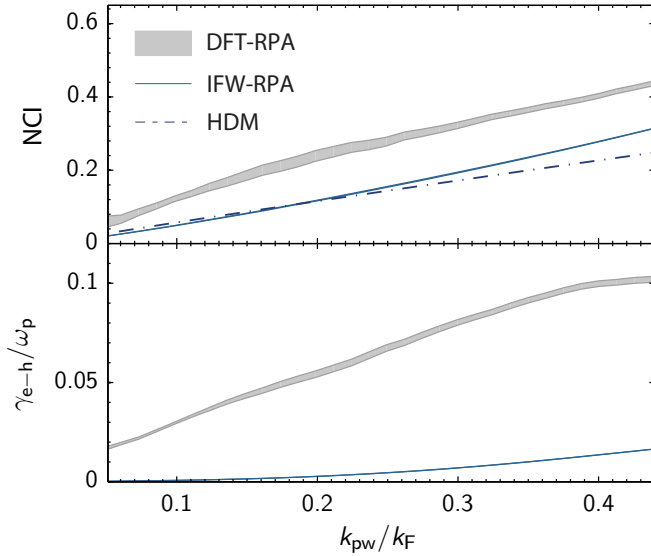


FIG. 6. (Upper panel) The NCI for the symmetric surface PWMs in Fig. 5 contrasting the HDM, the IFW-RPA, and the DFT-RPA results. (Lower panel) γ_{e-h} , the damping rate of the surface PWMs contributed from the e-h pair excitations contrasting the IFW-RPA and the DFT-RPA. The DFT-RPA results are illustrated as stripes, with the vertical width representing the numerical uncertainty of determining the quality factor of the PWM.

considered in Fig. 5, contrasting the HDM, the IFW-RPA, and the DFT-RPA. To compute the NCI in the RPA, the quality factor of the PWMs is needed. While this is indeed feasible, we note that the numerical determination of the quality factor comes with a small numerical uncertainty, especially for the DFT-RPA (see Appendix A for details). To visualize the numerical accuracy, the NCI for the DFT-RPA is accompanied by a shaded region representing the numerical uncertainty. The IFW-RPA gives an NCI close to that of the HDM, which is consistent with the agreement of their mode dispersions in Fig. 5. This suggests that the nonclassical energy of the PWMs in the IFW-RPA is mainly in the form of the hydrodynamic-like nonclassical kinetic energy. The DFT-RPA reveals a higher value of the NCI, which underlines the account for extra nonclassical degrees of freedom. It is reasonable to deduce that such extra degrees of freedom are associated with the finite work function and the associated electron spill-out, which constitute the main difference between the DFT-RPA and the other two models. As an evidence for this, we also plot the damping rate γ_{e-h} due to e-h pair excitations in Fig. 6. It is seen that γ_{e-h} is higher within the DFT-RPA than in the IFW-RPA. Thus, for the DFT-RPA, the proportion of energy carried by the e-h pairs is larger, which of course in turn serves to increase the NCI. However, a quantitative estimate of how many percentages of the NCI is contributed from the e-h excitations is technically difficult due to the complicated form of the RPA response function, and deserves a future study.

B. 2D metallic monolayer

In Sec. IV, we discussed the fundamental ceiling k_p to the wave number of PWMs as described within the HDM.

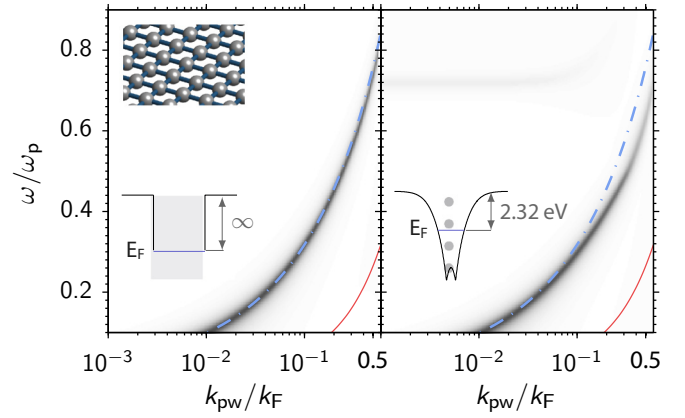


FIG. 7. Dispersions of the symmetric PWMs for a metallic 2D atomic monolayer. The results are computed within the HDM (dash-dotted lines), the IFW-RPA (left), and the DFT-RPA (right). The fundamental ceiling for the wave number k_p is also shown (solid lines). The atomic monolayer is chosen to represent the (100) surface of sodium, as illustrated in the inset in the left panel.

To approach this fundamental ceiling, it is preferable to have metallic waveguides with reduced transverse dimensions. Considering a metallic slab, the thinnest imaginable slab is conceptually that of a two-dimensional (2D) atomic monolayer [74]. In this subsection, we will investigate the PWMs of such a monolayer and discuss the practical feasibility of approaching k_p .

For the free-electron gas supported by a 2D atomic monolayer, the hydrodynamic equation, Eq. (2), requires a slight modifications owing to the dimensional reduction. In particular, \mathbf{J}_e and ρ_e in Eq. (2) are the induced electric current density and electric charge density on the 2D plane. Additionally, the Drude conductivity is expressed as $\sigma_D = in_{2D}/m_e(\omega + i\gamma)$ where n_{2D} is the equilibrium-electron density of the 2D monolayer. Furthermore, the nonlocal parameter β is $\sqrt{3/4}v_{2DF}$ for $\omega \gg \gamma$, and $\sqrt{1/2}v_{2DF}$ for $\omega \ll \gamma$, where v_{2DF} is the Fermi velocity of the 2D free-electron gas [75,76]. Besides the HDM, we also employ the IFW-RPA and the DFT-RPA to characterize the PWMs. In the IFW-RPA, the width of the infinite work function potential well t_{IFW} is chosen by $n_0 t_{IFW} = n_{2D}$. For the DFT-RPA, the ion pseudopotential proposed by Ashcroft [77] is used to describe the ion lattices beyond the jellium approximation. Finally, for numerical convenience we neglect the dependence of the pseudopotential on the 2D lattice by spatial averaging within the plan while preserving the out-of plane modulation of the potential (see right inset in Fig. 7).

The atomic monolayer of the (100) surface of sodium is taken as a thought example. Such a monolayer would have a square lattice with lattice constant $a_0 = 4.23 \text{ \AA}$ and accordingly $n_{2D} = 1/a_0^2$. Figure 7 depicts the dispersions of the symmetric PWMs, contrasting the HDM (dash-dotted lines), the IFW-RPA (left), and the DFT-RPA (right), and the ceiling wave number k_p (solid lines). With our eyes guided by the mode dispersion of the HDM, we observe that the results predicted by the HDM and the IFW-RPA have a good mutual agreement, while the mode dispersion of the DFT-RPA exhibits a redshifting and an enhanced damping as k_{pw} increases.

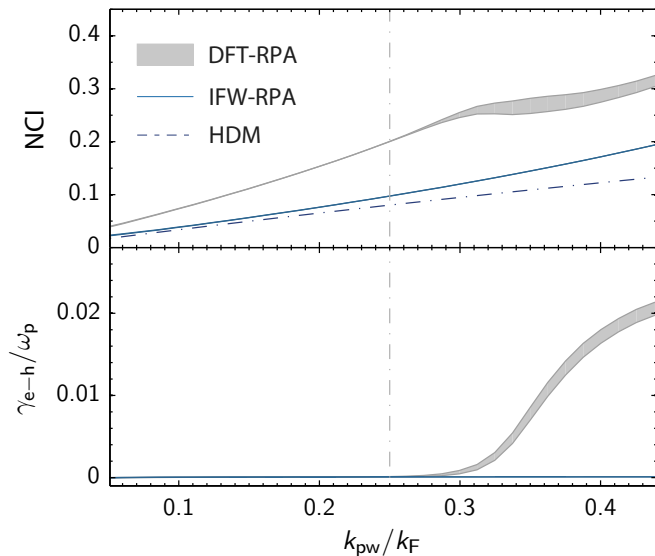


FIG. 8. The NCI (upper panel) for the symmetric PWMs considered in Fig. 7, contrasting the HDM, the IFW-RPA, and the DFT-RPA. The damping rate γ_{e-h} (lower panel) of the surface PWMs contributed from the e-h pair excitations, contrasting the IFW-RPA and the DFT-RPA. For the DFT-RPA results, the shaded region illustrates the numerical uncertainty of determining the quality factor of the PWM.

Additionally, we see that the fundamental ceiling wave number k_p is much larger than k_{pw} . This consolidates our previous statement that k_p mainly constitutes an ultimate limitation for plasmon focusing beyond the diffraction limit of light [57,63,78,79].

Figure 8 depicts the NCI for the PWMs in Fig. 7. Similar to our observations in Fig. 6, the values of the NCI are close to each other for the HDM and the IFW-RPA, while the DFT-RPA predicts a higher value due to the inclusion of additional nonclassical degrees of freedom. In Fig. 8 we also plot γ_{e-h} , contrasting the IFW-RPA and the DFT-RPA. We see that γ_{e-h} for the IFW-RPA is nearly zero and this also holds approximately in the DFT-RPA for k_{pw} smaller than $0.25k_F$ (marked by the vertical dash-dotted line). The reason is that the plasmon dynamics of such a monolayer resembles the intraband dynamics of an ideal 2D electron gas as long as the excitation energy is smaller than the minimum energy E_{int} required for e-h interband excitations. For the IFW-RPA the energy should exceed $E_{int} = 63.9$ eV, while for DFT-RPA the energy is much reduced to $E_{int} = 1.8$ eV. Accordingly, when the energy is smaller than E_{int} , the e-h pair excitations can only originate from intraband excitations, which is impossible for $k_{pw} < \omega/v_{F2D}$ [19]. For the DFT-RPA, the e-h interband excitations are possible when the excitation energy exceeds 1.8 eV, and can be further enhanced as the excitation energy approaches and eventually exceeds the work function of 2.32 eV. This explains our observations discussed earlier in this paper: the γ_{e-h} remains low unless $k_{pw} > 0.25k_F$, in which case the excitation energy favors noticeable e-h interband excitations. Finally, it is interesting to note that the numerical uncertainties of the NCI and γ_{e-h} exhibit a correlation with the magnitude of γ_{e-h} , which is discussed in more detail in Appendix A.

As another example of a 2D material, we briefly discuss doped graphene nanostructures [80]. On the one hand, classical electrodynamics will be unable to resolve atomic-scale details. On the other hand, the underlying graphene lattice can in fact be cut into flakes in two distinct different ways which host slightly different electronic properties: flakes where edge-atoms are configured in either an armchair or zigzag fashion. The latter gives rise to localized electronic edge states not supported by the former. These zigzag edge-states host additional optical transitions not found for armchair structures [40]. This is indeed also seen for the plasmon spectra of ribbons [39] and triangularly shaped flakes [41], where zigzag structures exhibit additional quantum dynamics not exhibited by the armchair counterparts [40]. In fact, the different magnitude in loss functions reported in Ref. [41] are in agreement with our anticipation that the zigzag structures exhibit a larger NCI than their armchair counterparts.

VI. DISCUSSION

The numerical results of the PWMs for a metallic slab show an excellent agreement between the HDM and the IFW-RPA; see Figs. 5 and 7. Is this just by pure coincidence or is it a manifestation of two more closely connected approaches? Here, we argue that the latter is indeed the case. We note that a formal relation between the HDM and the RPA is already established in Sec. IIB of Ref. [81], while in Appendix C we revisit the problem to offer a more explicit connection between the HDM and the IFW-RPA.

It should be emphasized that the (semi-)infinite electron gas obviously does not support any discretization of electron orbitals, i.e., quantum-size effects associated with the particle-in-a-box picture [82]. For an arbitrary confined electron gas occupying a finite region of space, quantum size effects would be captured in the RPA of the bounded electron gas, but not in the corresponding HDM. This can lead to an additional discrepancy between the HDM and RPA for the bounded electron gas. However, only minor differences are to be anticipated if quantum confinement is limited, i.e., for dimensions of the metal volume significantly exceeding the Fermi wavelength.

For noble metals, the Fermi wavelength is subnanometric ($\lambda_F \sim 0.5$ nm), and in few-nanometer sized metal particles thermal smearing would typically exceed the level spacing of the particle-in-a-box picture. For weakly doped semiconductors and low-dimensional materials, the Fermi wavelength can be much longer and quantization effects can indeed appear (quantized conductance is a famous consequence of this [83,84]). Additionally, in the extreme case like a 2D monolayer where strong out-of-plane quantum confinement may serve to only have electrons occupying a single 2D subband, the HDM for a 2D in-plane bounded electron gas again serves the k^2 approximation of the RPA for the corresponding bounded electron problem. From this perspective, the observed numerical agreement between the HDM and the IFW-RPA in Figs. 5 and 7 is to be expected. For doped graphene nanostructures (without edge-state contributions associated with zigzag edge termination) we have also reported similar good agreement between HDM and RPA [40].

VII. CONCLUSIONS

In conclusion, we have proposed a *nonclassical-impact parameter* (NCI) to quantify the nonclassical effects of plasmon resonances from an energy perspective. Importantly, we have provided a general expression for the NCI which links up to quantities commonly employed within classical electrodynamics in the discussion of plasmon resonances: the loss function and the quality factor. We have discussed the relation between the limiting value of the NCI and the electron-pressure wave in the hydrodynamic Drude model (HDM) and explored the ultimate ceiling to the confinement of the plasmon waveguiding modes. Guided by the NCI, nonclassical effects have been explored numerically for plasmon waveguiding modes, contrasting the HDM and the microscopic random-phase approximation (RPA). Finally, we have detailed the formal relation between the HDM and the RPA for a metal slab represented as an infinite work function potential well.

ACKNOWLEDGMENTS

We acknowledge Thomas Christensen for catalyzing our conceptual development of the nonclassical-impact parameter and thank Martijn Wubs for insightful comments on our manuscript. The Center for Nanostructured Graphene is sponsored by the Danish National Research Foundation, Project No. DNRF58. The work was also supported by the Danish Council for Independent Research-Natural Sciences, Project No. 1323-00087. W.Y. is financially supported by the Lundbeck Foundation, Grant No. 70802.

APPENDIX A: DERIVATION OF EQ. (1)

For plasmon resonances, the total energy U_T and the power dissipation P_L are related by the quality factor Q_{PR} through the relation

$$U_T = \frac{P_L Q_{PR}}{\omega_{PR}}. \quad (\text{A1})$$

Thus, we already see how the quality factor enters Eq. (4). Next, as mentioned in Sec V, plasmon resonances relate with the eigenstate of the dielectric function operator $\boldsymbol{\varepsilon}$, which in its spectral representation can be expressed as [59,60]

$$\boldsymbol{\varepsilon}(\omega) = \sum_n \varepsilon_n(\omega) |\phi_n(\omega)\rangle \langle \tilde{\rho}_n(\omega)|.$$

Here $|\phi_n(\omega)\rangle$ represents the eigenstate of $\boldsymbol{\varepsilon}$. The $|\phi_n(\omega)\rangle$ and $|\rho_n(\omega)\rangle$ satisfy the potential-density relation

$$\nabla \cdot \varepsilon_d(\mathbf{r}) \nabla \langle \mathbf{r} | \phi_n(\omega) \rangle = - \frac{\langle \tilde{\rho}_n(\omega) | \mathbf{r} \rangle}{\varepsilon_0}.$$

Among $|\phi_n(\omega)\rangle$, the electric potential state of the plasmon resonance is denoted as $|\phi_{PR}(\omega_{PR})\rangle$. The eigenvalue is $|\rho_{PR}\rangle$ with $\text{Im}[\varepsilon_{PR}^{-1}]$ exhibiting a peak at ω_{PR} . The related electron charge density state $|\rho_{PR}\rangle$ at ω_{PR} is defined by

$$|\rho_{PR}\rangle = \langle \tilde{\rho}_{PR} |.$$

Next, consider an arbitrary external electric potential state $|\phi_{ext}\rangle$ at the resonant frequency ω_{PR} incident on the plasmonic structure. The induced potential state of plasmon resonances,

denoted as $|\phi_{PR}^i\rangle$, has the expression

$$|\phi_{PR}^i\rangle = \varepsilon_{PR}^{-1} \frac{\langle \tilde{\rho}_{PR} | \phi_{ext} \rangle}{\langle \tilde{\rho}_{PR} | \phi_{PR} \rangle} |\phi_{PR}\rangle.$$

The dissipation energy contributed from $|\phi_{PR}^i\rangle$ is

$$P_L = -\frac{1}{2} \text{Im} \left[\varepsilon_{PR}^{-1} \omega_{PR} \frac{\langle \tilde{\rho}_{PR} | \phi_{ext} \rangle}{\langle \tilde{\rho}_{PR} | \phi_{PR} \rangle} \langle \phi_{ext} | \rho_{PR} \rangle \right], \quad (\text{A2})$$

and the electric field energy associated with $|\phi_{PR}^i\rangle$ is

$$U_E = \frac{1}{4} |\varepsilon_{PR}^{-1}|^2 \left| \frac{\langle \tilde{\rho}_{PR} | \phi_{ext} \rangle}{\langle \tilde{\rho}_{PR} | \phi_{PR} \rangle} \right|^2 \langle \phi_{PR} | \rho_{PR} \rangle. \quad (\text{A3})$$

With Eq. (A1), expressions for P_L and U_T can be derived and Eq. (4) is eventually rewritten as

$$\text{NCI} = 1 - \frac{1}{Q_{PR}} \text{Im} \left[(\varepsilon_{PR}^{-1})^* \frac{\langle \phi_{ext} | \rho_{PR} \rangle \langle \phi_{PR} | \tilde{\rho}_{PR} \rangle}{\langle \phi_{ext} | \tilde{\rho}_{PR} \rangle \langle \phi_{PR} | \rho_{PR} \rangle} \right]. \quad (\text{A4})$$

To excite plasmon resonances, the most efficient way is to choose $|\phi_{ext}\rangle \propto |\phi_{PR}\rangle$. In this way we finally arrive at Eq. (1).

We note that the NCI is an intrinsic property of plasmon resonances, and should be independent of the external potential. However, the NCI in Eq. (A4) shows a dependence on the external potential, and Eq. (1) is derived with a special choice of $|\phi_{ext}\rangle$. This is because $|\phi_{PR}\rangle$ is only a close approximation to plasmon resonances with losses. Evidently, if the loss is zero, we have $|\rho_{PR}\rangle = |\tilde{\rho}_{PR}\rangle$, and the dependence on the external potential of the NCI is removed. The final expression of the NCI is again Eq. (1).

To compute the NCI, Q_{PR} and $\text{Im}[\varepsilon_{PR}^{-1}]$ are needed. $\text{Im}[\varepsilon_{PR}^{-1}]$ can be directly computed by solving the eigenvalues of the operator $\boldsymbol{\varepsilon}$. For Q_{PR} , it can be expressed as

$$Q_{PR} = \frac{\omega_{PR}}{\gamma_{PR}}, \quad (\text{A5})$$

with γ_{PR} defined as the resonance width of $-\text{Im}[\varepsilon_{PR}^{-1}]$. To determine γ_{PR} , we use a Lorentzian function to fit the spectrum of $\text{Im}[\varepsilon_n^{-1}(\omega)]$, and the width of the fitted Lorentzian function is γ_{PR} . From the numerical observations, it is found that such a scheme to determine γ_{PR} is appropriate for the IFW-RPA with the fitting error below 1%. However, for the DFT-RPA, the fitting error for parameters in Figs. 6 and 8 is larger with the highest value approaching approximately 4%. The fitting error gives the numerical uncertainty of γ_{PR} , which is visualized by the shaded regions in Figs. 6 and 8. Further, we deduce that the larger fitting error in the DFT-RPA is related to the stronger e-h excitations, which distort the resonance spectrum from the Lorentzian shape. The deduction is indirectly evidenced by the observations in Fig. 8 that the numerical uncertainty increases with γ_{e-h} .

APPENDIX B: PROOF OF EQ. (7)

To prove Eq. (7), we first rewrite Eq. (2) in terms of the polarization field \mathbf{P} defined by $\mathbf{P} = i\varepsilon_0 \mathbf{J}_e / \omega$ and the electric field \mathbf{E} :

$$\mathbf{P} + \frac{\beta^2}{\omega^2} \nabla \nabla \cdot \mathbf{P} = -\frac{\omega_p^2}{\omega^2} \mathbf{E}. \quad (\text{B1})$$

Here, we have without loss of generality suppressed the damping γ . Next, by applying the operation $\int ds_m P_z^* \hat{\mathbf{z}} \cdot$ to

both sides of Eq. (B1) we arrive at

$$k_{\text{pw}}^2 = k_{\text{p}}^2 + \frac{\int ds_{\text{m}} \omega_{\text{p}}^2 E_z P_z^* / \beta^2 - ik_{\text{pw}} \mathbf{P}_{\parallel} \cdot \nabla_{\parallel} P_z^*}{\int ds_{\text{m}} |P_z|^2}. \quad (\text{B2})$$

Here, the cross-sectional plane of the waveguide is chosen to be the x - y plane and subscripts are used to indicate vector components parallel to the cross-sectional plane. To derive Eq. (B2), we employed the additional boundary condition that the normal component of \mathbf{P} is vanishing at the boundary. Next, we focus on the integrand (in the following denoted by p) in the numerator on the right-hand side of Eq. (B2):

$$p = \frac{\omega_{\text{p}}^2}{\beta^2} p_1 + p_2, \quad (\text{B3})$$

where

$$p_1 = \int ds_{\text{m}} E_z P_z^*,$$

$$p_2 = \int ds_{\text{m}} -ik_{\text{pw}} \mathbf{P}_{\parallel} \cdot \nabla_{\parallel} P_z^*.$$

For p_1 , we may write the electrical field as $E_z = -ik_{\text{pw}}\phi$, where ϕ represents the electric potential, and for the polarization we have $P_z = ik_{\text{pw}}\phi\omega_{\text{p}}^2/\omega^2 - ik_{\text{pw}}\nabla^2\phi\beta^2/\omega^2$ from Eq. (B1). In this way we have

$$p_1 = - \int ds_{\text{m}} \left(\frac{k_{\text{pw}}^4 \beta^2 + k_{\text{pw}}^2 \omega_{\text{p}}^2}{\omega^2} |\phi|^2 - \frac{k_{\text{pw}}^2 \beta^2}{\omega^2} \phi \nabla_{\parallel}^2 \phi^* \right).$$

Using the identity $\phi \nabla_{\parallel}^2 \phi^* = \nabla_{\parallel} \cdot (\phi \nabla_{\parallel} \phi^*) - |\nabla_{\parallel} \phi|^2$, the integral $\int ds_{\text{m}} \phi \nabla_{\parallel}^2 \phi^*$ is found to be

$$- \int ds_{\text{m}} |\nabla_{\parallel} \phi|^2 + \oint dl_{\text{m}} \phi_{\parallel} \nabla \phi^* \cdot \hat{\mathbf{n}}.$$

Here, $\oint dl_{\text{m}}$ is the integration along the boundary of the metal side, and $\hat{\mathbf{n}}$ is the surface normal pointing outward the metal. Employing the boundary conditions that $\phi_{\text{m}} = \phi_{\text{d}}$ and $\nabla_{\parallel} \phi_{\text{m}} \cdot \hat{\mathbf{n}} = \varepsilon_{\text{d}} \nabla_{\parallel} \phi_{\text{d}} \cdot \hat{\mathbf{n}}$, where the subscripts ‘‘m’’ and ‘‘d’’ indicate the quantities at the boundary belonging to the metal and the embedding dielectric medium, respectively, the integration $\oint dl_{\text{m}} \phi_{\parallel} \nabla \phi^* \cdot \hat{\mathbf{n}}$ can be rewritten as

$$\int ds_{\text{d}} \varepsilon_{\text{d}} (|\nabla_{\parallel} \phi|^2 + \varepsilon_{\text{d}} k_{\text{pw}}^2 |\phi|^2).$$

In summary, we have

$$p_1 = - \int ds_{\text{m}} \left(\frac{k_{\text{pw}}^4 \beta^2 + k_{\text{pw}}^2 \omega_{\text{p}}^2}{\omega^2} |\phi|^2 + \frac{k_{\text{pw}}^2 \beta^2}{\omega^2} |\nabla_{\parallel} \phi|^2 \right)$$

$$- \int ds_{\text{m}} \left(\frac{\varepsilon_{\text{d}} k_{\text{pw}}^4 \beta^2}{\omega^2} |\phi|^2 + \frac{\varepsilon_{\text{d}} k_{\text{pw}}^2 \beta^2}{\omega^2} |\nabla_{\parallel} \phi|^2 \right).$$

For the dielectric background with $\varepsilon_{\text{d}} > 0$, it is clear that $p_1 < 0$.

Next, we turn to p_2 . The potential ϕ in the metal can be decomposed into the transverse component ϕ^{T} and the longitudinal component ϕ^{L} , respectively. These potentials satisfy $\nabla^2 \phi^{\text{T}} = 0$ and $\nabla^2 \phi^{\text{L}} + k_{\text{L}}^2 \phi^{\text{L}} = 0$, where $k_{\text{L}} = \sqrt{\omega^2 - \omega_{\text{p}}^2}/\beta$.

In terms of ϕ^{T} and ϕ^{L} , \mathbf{P} is expressed as

$$\mathbf{P} = (\nabla_{\parallel} + ik_{\text{pw}} \hat{\mathbf{z}}) \left[\frac{\omega_{\text{p}}^2}{\omega^2} \phi^{\text{T}} + \phi^{\text{L}} \right].$$

The above expression directly leads to

$$p_2 = - \int ds_{\text{m}} k_{\text{pw}}^2 \left| \frac{\omega_{\text{p}}^2}{\omega^2} \nabla_{\parallel} \phi^{\text{T}} + \nabla_{\parallel} \phi^{\text{L}} \right|^2,$$

which implies that $p_2 < 0$. With Eq. (B2) and the inequalities $p_1 < 0$ and $p_2 < 0$, we now finally arrive at Eq. (7).

APPENDIX C: HDM VERSUS IFW-RPA

First, consider an extended electron gas with a uniform equilibrium-electron density. In this case, it is known that the HDM is the k^2 approximation of the RPA. We represent this symbolically as

$$\text{RPA}_0 \xrightarrow{k^2 \text{ approx.}} \text{HDM}_0. \quad (\text{C1})$$

with the subscript reminding us of the underlying equilibrium assumption of an infinite homogenous electron gas.

Next, consider the bounded electron gas, where the spatial extension is now finite. In this case, the HDM assumes a uniform equilibrium electron density while the act of an infinite work function is incorporated in the equations through an additional boundary condition that accounts for the vanishing electron flux through the surface of the metal. For clarity, we symbolically denote this model as ‘‘HDM_b’’ in order to clearly distinguish it from the case of the infinite electron gas. To establish the relation between the HDM_b and the RPA, we turn to the HDM_b in an integral form,

$$\rho_{\text{e}}(\mathbf{r}) = \int d\mathbf{r}' \chi_{\text{HDM}_b}(\omega, \mathbf{r}, \mathbf{r}') [e^2 \phi(\mathbf{r}')],$$

resembling the form within the RPA. For an arbitrary electron gas, we do not find a general way to derive the expression of χ_{HDM_b} . To make progress, we put the generality aside and focus on the specific case of a semi-infinite electron gas with a planar boundary. The new light shed by this specific example will then guide us to a more general conclusion. The semi-infinite electron gas is located at $x \leq 0$. With Eq. (2) and the additional boundary condition, χ_{HDM_b} is then derived:

$$\chi_{\text{HDM}_b}(\omega, \mathbf{r}, \mathbf{r}') = \chi_{\text{HDM}_0}(\omega, \mathbf{r}, \mathbf{r}') + \chi_{\text{HDM}_0}(\omega, \mathbf{r}, \mathcal{P}_x \mathbf{r}'). \quad (\text{C2})$$

Here, χ_{HDM_0} is the response function of the HDM for the infinite homogenous electron gas and \mathcal{P}_x is the parity operator on the x coordinate defined by $\mathcal{P}_x \mathbf{r} = \{-x, y, z\}$. The first response function has the expression

$$\chi_{\text{HDM}_0}(\omega, \mathbf{r}, \mathbf{r}') = - \frac{n_0}{m_e \beta^2} \delta(\mathbf{r} - \mathbf{r}') - \frac{n_0 k_{\text{p}}^2}{4\pi m_e \beta^2 |\mathbf{r} - \mathbf{r}'|} e^{ik_{\text{p}}|\mathbf{r} - \mathbf{r}'|},$$

where k_{p} is the wave number of the electron-pressure wave defined in Eq. (6). Eqs. (C1) and (C2) together suggest that the HDM_b can be considered the k^2 approximation of a specific RPA denoted as RPA_b, with the response function χ_{RPA_b}

being

$$\chi_{\text{RPA}_b}(\omega, \mathbf{r}, \mathbf{r}') = \chi_{\text{RPA}_0}(\omega, \mathbf{r}, \mathbf{r}') + \chi_{\text{RPA}_0}(\omega, \mathbf{r}, \mathcal{P}_x \mathbf{r}'). \quad (\text{C3})$$

Here, χ_{RPA_0} is the response function of the RPA for the infinite homogenous electron gas. With the expression of χ_{RPA_0} , the χ_{RPA_b} can be written as

$$\chi_{\text{RPA}_b} = \frac{\chi_{\text{IFW}}}{2} + \frac{\chi_{\text{ZMB}}}{2}, \quad (\text{C4})$$

with χ_{IFW} being the response function for the IFW-RPA, whose physical meaning is presented in Sec. V. In the second term, χ_{ZMB} is the response function for the bounded electron gas satisfying the boundary condition that the normal component of the derivative of the electron wave function is vanishing at the surface. This boundary condition is mathematically well defined, provided that the electron mass approaches zero at the boundary, i.e., a *zero-mass boundary* (ZMB). The relation between the HDM_b and the RPA_b for the semi-infinite electron

gas can now be symbolically summarized as

$$\frac{\text{IFW-RPA}}{2} + \frac{\text{ZMB-RPA}}{2} \xrightarrow{k^2 \text{ approx.}} \text{HDM}_b. \quad (\text{C5})$$

Below, we provide an intuitive shortcut to better appreciate Eq. (C5). First, in the IFW-RPA and the ZMB-RPA, the electron wave functions ψ are determined by the boundary conditions $\psi_{\text{IFW}}(x=0) = 0$ and $\partial\psi_{\text{ZMB}}(x=0)/\partial x = 0$, respectively. Thus, we have $\psi_{\text{IFW}} \propto \sin(k_x x)e^{i\mathbf{k}_{\parallel} \cdot \mathbf{r}_{\parallel}}$ and $\psi_{\text{ZMB}} \propto \cos(k_x x)e^{i\mathbf{k}_{\parallel} \cdot \mathbf{r}_{\parallel}}$, where the subscripts indicate the parallel components of the vectors in the y - z plane. The wave functions ensure that the normal component of the electron current vanishes at the boundary, which is consistent with the additional boundary condition in the HDM_b . Additionally, a uniform equilibrium electron density is assumed within the HDM_b . This feature is respected by the average of the equilibrium electron density of the IFW-RPA and the ZMB-RPA, i.e., $n_0(x) \propto |\psi_{\text{IFW}}|^2 + |\psi_{\text{ZMB}}|^2 \propto \cos^2(k_x x) + \sin^2(k_x x) \propto \text{constant}$. Thus, important features of the HDM_b are all covered by the average of the IFW-RPA and the ZMB-RPA, which highlights the validity of Eq. (C5).

-
- [1] S. A. Maier, *Plasmonics: Fundamentals and Applications* (Springer, New York, 2007).
- [2] D. K. Gramotnev and S. I. Bozhevolnyi, *Nat. Photon.* **4**, 83 (2010).
- [3] J. A. Schuller, E. S. Barnard, W. S. Cai, Y. C. Jun, J. S. White, and M. L. Brongersma, *Nat. Mater.* **9**, 193 (2010).
- [4] M. L. Brongersma, *Faraday Discuss.* **178**, 9 (2015).
- [5] A. Baev, P. N. Prasad, H. Ågren, M. Samoć, and M. Wegener, *Phys. Rep.* **594**, 1 (2015).
- [6] D. P. O'Neal, L. R. Hirsch, N. Halas, J. D. Payne, and J. L. West, *Cancer Lett.* **209**, 171 (2004).
- [7] K. C. Huang, M.-K. Seo, T. Sarmiento, Y. Huo, J. S. Harris, and M. L. Brongersma, *Nat. Photon.* **8**, 244 (2014).
- [8] C. L. C. Smith, N. Stenger, A. Kristensen, N. A. Mortensen, and S. I. Bozhevolnyi, *Nanoscale* **7**, 9355 (2015).
- [9] M. A. Noginov, G. Zhu, A. M. Belgrave, V. M. Bakker, V. M. Shalaev, E. E. Narimanov, S. Stout, E. Herz, T. Suteewong, and U. Wiesner, *Nature (London)* **460**, 1110 (2009).
- [10] R. F. Oulton, V. J. Sorger, T. Zentgraf, R.-M. Ma, C. Gladden, L. Dai, G. Bartal, and X. Zhang, *Nature (London)* **461**, 629 (2009).
- [11] D. E. Chang, A. S. Sørensen, E. A. Demler, and M. D. Lukin, *Nat. Phys.* **3**, 807 (2007).
- [12] S. Raza, S. I. Bozhevolnyi, M. Wubs, and N. A. Mortensen, *J. Phys. Condens. Matter* **27**, 183204 (2015).
- [13] J. Kern, S. Grossmann, N. V. Tarakina, T. Häckel, M. Emmerling, M. Kamp, J.-S. Huang, P. Biagioni, J. Prangasma, and B. Hecht, *Nano Lett.* **12**, 5504 (2012).
- [14] K. J. Savage, M. M. Hawkeye, R. Esteban, A. G. Borisov, J. Aizpurua, and J. J. Baumberg, *Nature (London)* **491**, 574 (2012).
- [15] J. A. Scholl, A. Garcia-Etxarri, A. L. Koh, and J. A. Dionne, *Nano Lett.* **13**, 564 (2013).
- [16] S. Raza, N. Stenger, A. Pors, T. Holmgaard, S. Kadkhodazadeh, J. B. Wagner, K. Pedersen, M. Wubs, S. I. Bozhevolnyi, and N. A. Mortensen, *Nat. Commun.* **5**, 4125 (2014).
- [17] J. Kern, R. Kulklock, J. Prangasma, M. Emmerling, M. Kamp, and B. Hecht, *Nat. Photon.* **9**, 582 (2015).
- [18] M. S. Tame, K. R. McEnery, S. K. Oezdemir, J. Lee, S. A. Maier, and M. S. Kim, *Nat. Phys.* **9**, 329 (2013).
- [19] H. Bruus and K. Flensberg, *Many-body Quantum Theory in Condensed Matter Physics: An Introduction* (Oxford University Press, Oxford, 2004).
- [20] S. Raza, G. Toscano, A.-P. Jauho, M. Wubs, and N. A. Mortensen, *Phys. Rev. B* **84**, 121412(R) (2011).
- [21] N. Lang and W. Kohn, *Phys. Rev. B* **1**, 4555 (1970).
- [22] D. F. Jin, Q. Hu, D. Neuhauser, F. von Cube, Y. Y. Yang, R. Sachan, T. S. Luk, D. C. Bell, and N. X. Fang, *Phys. Rev. Lett.* **115**, 193901 (2015).
- [23] W. Yan, M. Wubs, and N. Asger Mortensen, *Phys. Rev. Lett.* **115**, 137403 (2015).
- [24] N. A. Mortensen, S. Raza, M. Wubs, T. Søndergaard, and S. I. Bozhevolnyi, *Nat. Commun.* **5**, 3809 (2014).
- [25] F. J. García de Abajo, *J. Phys. Chem. C* **112**, 17983 (2008).
- [26] D. Marinica, A. Kazansky, P. Nordlander, J. Aizpurua, and A. Borisov, *Nano Lett.* **12**, 1333 (2012).
- [27] R. Esteban, A. Borisov, P. Nordlander, and J. Aizpurua, *Nat. Commun.* **3**, 825 (2012).
- [28] L. Stella, P. Zhang, F. García-Vidal, A. Rubio, and P. García-González, *J. Phys. Chem. C* **117**, 8941 (2013).
- [29] T. V. Teperik, P. Nordlander, J. Aizpurua, and A. G. Borisov, *Phys. Rev. Lett.* **110**, 263901 (2013).
- [30] V. Kulkarni and A. Manjavacas, *ACS Photonics* **2**, 987 (2015).
- [31] E. Townsend, A. Debrecht, and G. W. Bryant, *J. Mater. Res.* **30**, 2389 (2015).
- [32] J. A. Scholl, A. L. Koh, and J. A. Dionne, *Nature (London)* **483**, 421 (2012).
- [33] C. Ciraci, R. T. Hill, J. J. Mock, Y. Urzhumov, A. I. Fernández-Domínguez, S. A. Maier, J. B. Pendry, A. Chilkoti, and D. R. Smith, *Science* **337**, 1072 (2012).
- [34] S. Raza, N. Stenger, S. Kadkhodazadeh, S. V. Fischer, N. Kotesha, A.-P. Jauho, A. Burrows, M. Wubs, and N. A. Mortensen, *Nanophotonics* **2**, 131 (2013).

- [35] J. Mertens, A. L. Eiden, D. O. Sigle, F. Huang, A. Lombardo, Z. Sun, R. S. Sundaram, A. Colli, C. Tserkezis, J. Aizpurua, S. Milana, A. C. Ferrari, and J. J. Baumberg, *Nano Lett.* **13**, 5033 (2013).
- [36] S. F. Tan, L. Wu, J. K. W. Yang, P. Bai, M. Bosman, and C. A. Nijhuis, *Science* **343**, 1496 (2014).
- [37] S. Raza, S. Kadkhodazadeh, T. Christensen, M. Di Vece, M. Wubs, N. A. Mortensen, and N. Stenger, *Nat. Commun.* **6**, 8788 (2015).
- [38] H. Jung, H. Cha, D. Lee, and S. Yoon, *ACS Nano* **9**, 12292 (2015).
- [39] S. Thongrattanasiri, A. Manjavacas, and F. J. García de Abajo, *ACS Nano* **6**, 1766 (2012).
- [40] T. Christensen, W. H. Wang, A.-P. Jauho, M. Wubs, and N. A. Mortensen, *Phys. Rev. B* **90**, 241414(R) (2014).
- [41] W. H. Wang, T. Christensen, A.-P. Jauho, K. S. Thygesen, M. Wubs, and N. A. Mortensen, *Sci. Rep.* **5**, 9535 (2015).
- [42] H. Harutyunyan, A. B. F. Martinson, D. Rosenmann, L. K. Khorashad, L. V. Besteiro, A. O. Govorov, and G. P. Wiederrecht, *Nat. Nanotechnol.* **10**, 770 (2015).
- [43] M. L. Brongersma, N. J. Halas, and P. Nordlander, *Nat. Nanotechnol.* **10**, 25 (2015).
- [44] C. Voisin, D. Christofilos, N. Del Fatti, F. Vallée, B. Prével, E. Cottancin, J. Lermé, M. Pellarin, and M. Broyer, *Phys. Rev. Lett.* **85**, 2200 (2000).
- [45] P. J. Feibelman, *Prog. Surf. Sci.* **12**, 287 (1982).
- [46] P. Apell and D. R. Penn, *Phys. Rev. Lett.* **50**, 1316 (1983).
- [47] K. D. Tsuei, E. W. Plummer, A. Liebsch, E. Pehlke, K. Kempa, and P. Bakshi, *Surf. Sci.* **247**, 302 (1991).
- [48] I. A. Larkin and M. I. Stockman, *Nano Lett.* **5**, 339 (2005).
- [49] A. Wiener, A. I. Fernández-Domínguez, A. P. Horsfield, J. B. Pendry, and S. A. Maier, *Nano Lett.* **12**, 3308 (2012).
- [50] J. B. Khurgin, *Faraday Discuss.* **178**, 109 (2015).
- [51] G. Toscano, S. Raza, A.-P. Jauho, M. Wubs, and N. A. Mortensen, *Opt. Express* **20**, 4176 (2012).
- [52] A. I. Fernández-Domínguez, A. Wiener, F. J. García-Vidal, S. A. Maier, and J. B. Pendry, *Phys. Rev. Lett.* **108**, 106802 (2012).
- [53] I. Romero, J. Aizpurua, G. W. Bryant, and F. J. García de Abajo, *Opt. Express* **14**, 9988 (2006).
- [54] M. M. Özer, E. J. Moon, A. G. Eguiluz, and H. H. Weitering, *Phys. Rev. Lett.* **106**, 197601 (2011).
- [55] G. Toscano, S. Raza, W. Yan, C. Jeppesen, S. Xiao, M. Wubs, A.-P. Jauho, S. I. Bozhevolnyi, and N. A. Mortensen, *Nanophotonics* **2**, 161 (2013).
- [56] Q. Huang, F. Bao, and S. He, *Opt. Express* **21**, 1430 (2013).
- [57] S. Raza, T. Christensen, M. Wubs, S. I. Bozhevolnyi, and N. A. Mortensen, *Phys. Rev. B* **88**, 115401 (2013).
- [58] M. Ichikawa, *J. Phys. Soc. Jpn.* **80**, 044606 (2011).
- [59] K. Andersen, K. W. Jacobsen, and K. S. Thygesen, *Phys. Rev. B* **86**, 245129 (2012).
- [60] K. Andersen, K. L. Jensen, N. A. Mortensen, and K. S. Thygesen, *Phys. Rev. B* **87**, 235433 (2013).
- [61] F. J. García de Abajo, *Rev. Mod. Phys.* **82**, 209 (2010).
- [62] P. Halevi, *Phys. Rev. B* **51**, 7497 (1995).
- [63] W. Yan, M. Wubs, and N. A. Mortensen, *Phys. Rev. B* **86**, 205429 (2012).
- [64] G. Toscano, J. Straubel, A. Kwiatkowski, C. Rockstuhl, F. Evers, H. Xu, N. A. Mortensen, and M. Wubs, *Nat. Commun.* **6**, 7132 (2015).
- [65] W. Yan, *Phys. Rev. B* **91**, 115416 (2015).
- [66] X. Li, H. Fang, X. Weng, L. Zhang, X. Dou, A. Yang, and X. Yuan, *Opt. Express* **23**, 29738 (2015).
- [67] F. Wang and Y. R. Shen, *Phys. Rev. Lett.* **97**, 206806 (2006).
- [68] P. Jewsbury, *J. Phys. F* **11**, 195 (1981).
- [69] R. Slavch and R. Tsekov, *J. Chem. Phys.* **132**, 084505 (2010).
- [70] J. B. Khurgin, *Nat. Nanotechnol.* **10**, 2 (2015).
- [71] T. Christensen, W. Yan, S. Raza, A.-P. Jauho, N. A. Mortensen, and M. Wubs, *ACS Nano* **8**, 1745 (2014).
- [72] O. Keller, M. Xiao, and S. Bozhevolnyi, *Opt. Comm.* **102**, 238 (1993).
- [73] W. Kohn and L. J. Sham, *Phys. Rev.* **140**, A1133 (1965).
- [74] A. Manjavacas and F. J. García de Abajo, *Nat. Commun.* **5**, 3548 (2014).
- [75] A. L. Fetter, *Ann. Phys.* **81**, 367 (1973).
- [76] J. D. Jackson, *Classical Electrodynamics* (John Wiley & Sons, New Jersey, 1962).
- [77] N. W. Ashcroft, *Phys. Lett.* **23**, 48 (1966).
- [78] W. Yan, N. A. Mortensen, and M. Wubs, *Opt. Express* **21**, 15026 (2013).
- [79] C. David, N. A. Mortensen, and J. Christensen, *Sci. Rep.* **3**, 2526 (2013).
- [80] F. J. García de Abajo, *ACS Photonics* **1**, 135 (2014).
- [81] A. Eguiluz, *Phys. Rev. B* **19**, 1689 (1979).
- [82] F. J. García de Abajo, *Nature (London)* **483**, 417 (2012).
- [83] B. J. van Wees, H. van Houten, C. W. J. Beenakker, J. G. Williamson, L. P. Kouwenhoven, D. van der Marel, and C. T. Foxon, *Phys. Rev. Lett.* **60**, 848 (1988).
- [84] N. Tombros, A. Veligura, J. Junesch, M. H. D. Guimarães, I. J. Vera-Marun, H. T. Jonkman, and B. J. van Wees, *Nat. Phys.* **7**, 697 (2011).